*J. Fluid Mech.* (2007), *vol.* 585, *pp.* 395–420. © 2007 Cambridge University Press
doi:10.1017/S0022112007006763 Printed in the United Kingdom


# Effects of initial conditions in decaying turbulence generated by passive grids

P. LAVOIE†, L. DJENIDI AND R. A. ANTONIA
Discipline of Mechanical Engineering, University of Newcastle, NSW 2308, Australia

(Received 7 April 2006 and in revised form 30 March 2007)

The effects of initial conditions on grid turbulence are investigated for low to moderate Reynolds numbers. Four grid geometries are used to yield variations in initial conditions and a secondary contraction is introduced to improve the isotropy of the turbulence. The hot-wire measurements, believed to be the most detailed to date for this flow, indicate that initial conditions have a persistent impact on the large-scale organization of the flow over the length of the tunnel. The power-law coefficients, determined via an improved method, also depend on the initial conditions. For example, the power-law exponent $m$ is affected by the various levels of large-scale organization and anisotropy generated by the different grids and the shape of the energy spectrum at low wavenumbers. However, the results show that these effects are primarily related to deviations between the turbulence produced in the wind tunnel and true decaying homogenous isotropic turbulence (HIT). Indeed, when isotropy is improved and the intensity of the large-scale periodicity, which is primarily associated with round-rod grids, is decreased, the importance of initial conditions on both the character of the turbulence and $m$ is diminished. However, even in the case where the turbulence is nearly perfectly isotropic, $m$ is not equal to $-1$, nor does it show an asymptotic trend in $x$ towards this value, as suggested by recent analysis. Furthermore, the evolution of the second- and third-order velocity structure functions satisfies equilibrium similarity only approximately.

## 1. Introduction

Homogeneous and isotropic turbulence (HIT), arguably the simplest type of turbulence, is a fundamental flow in the study and development of turbulence theory and models. In their seminal work, von Kármán & Howarth (1938) derived the transport equation that relates the double ($\equiv B_{uu} = \langle u\,(x+r)\,u\,(x)\rangle$) and triple ($\equiv B_{uuu} = \langle u^2\,(x+r)\,u\,(x)\rangle$) streamwise velocity correlation functions for temporally decaying HIT:

$$\frac{\partial B_{uu}}{\partial t} + 2\left(\frac{\partial B_{uuu}}{\partial r} + 4\frac{B_{uuu}}{r}\right) = 2\nu\left(\frac{\partial^2 B_{uu}}{\partial r^2} + \frac{4}{r}\frac{\partial B_{uu}}{\partial r}\right). \tag{1.1}$$

Under certain assumptions, (1.1) can yield predictions about the decay of the turbulence. The most widely used technique to solve (1.1) has been to look for the solutions for which the correlation functions remain self-preserving throughout the decay, where self-preservation requires that the double and triple correlation functions collapse when they are normalized using a single length scale and a single

† Present address: Department of Aeronautics, Imperial College London, SW7 2AZ, UK.

velocity scale. A number of authors (e.g. Dryden 1943; Batchelor 1948; Korneyev & Sedov 1976) have investigated the solutions to (1.1) that admit a self-preserving form. These yielded the prediction, which is now commonly accepted, that the turbulent kinetic energy decays according to a power law of the form

$$\langle q^2 \rangle \sim (t - t_0)^m , \tag{1.2}$$

where $m$ is the power-law exponent and $t_0$ the virtual origin. The value of $m$ yielded by any given analysis, however, depends on the assumptions used. The classical solution for complete self-preservation at all scales (referred to herein simply as self-preservation) in the initial period of decay was found by Dryden (1943), and later derived in a more rigorous manner by Batchelor (1948). This solution requires $R_\lambda$ to remain constant throughout the decay, which leads to the prescription that $m = -1$, and is linked to the classical result that the decay of HIT is universal, owing to the conditions of homogeneity and isotropy.

Although early experimental work seems to support the prediction that $m = -1$ (e.g. Batchelor & Townsend 1948; Kistler & Vrebalovich 1966), later experiments, mainly those of Comte-Bellot & Corrsin (1966) (see also Mohamed & LaRue (1990) who reviewed much of the available data), have led to the present consensus that $m \leqslant -1$. Values of $m$ between $-1$ and $-1.75$ have been obtained experimentally (e.g. Uberoi & Wallis 1967; Ling & Wan 1972; Gad-el-Hak & Corrsin 1974, and references therein), whereas direct numerical simulation (DNS) of periodic three-dimensional box turbulence, which provides better approximations of decaying HIT than grid turbulence, has yielded a similar spread of values (e.g. de Bruyn Kops & Riley 1998; Wray 1998; Huang & Leonard 1994; Antonia & Orlandi 2004; Burattini *et al.* 2006). The origin of the large range of values found in both experiments and simulations remains a debated issue. Mohamed & LaRue (1990) attribute the scatter to inconsistencies in the methods used by different authors to determine the power-law exponent, whereas George (1992) argues that this reflects the dependence of $m$ on initial conditions. (The term 'initial conditions' is used here to refer to the conditions under which the turbulence was produced, either experimentally or numerically.) The importance of this issue with respect to turbulence models has been highlighted by George *et al.* (2001).

George's (1992) argument is based on a re-evaluation of classical self-preservation solutions, which have assumed from the outset that the same similarity scales should apply to the double and triple correlation functions. The main feature of the approach used by George is that the self-preservation assumption is relaxed so that the similarity scales emerge from the governing equation rather than being the result of *ad hoc* assumptions. George found that (1.1) admits different similarity scales for the second- and third-order functions. We draw a formal distinction between the approach described by George (1992), known as equilibrium similarity, and the self-preservation hypothesis of Dryden (1943), although both theories become fully equivalent for $R_\lambda \to \infty$. For convenience, we briefly introduce equilibrium similarity within the framework of the energy structure function equation as obtained by Danaila, Anselmet & Antonia (2002), that is,

$$-\langle (\delta u)(\delta q)^2 \rangle + 2\nu \frac{\mathrm{d}}{\mathrm{d}r} \langle (\delta q)^2 \rangle + I_q = \tfrac{4}{3} \langle \epsilon \rangle r, \tag{1.3}$$

where $\langle (\delta q)^2 \rangle \equiv \langle (\delta u)^2 \rangle + \langle (\delta v)^2 \rangle + \langle (\delta w)^2 \rangle$, $\langle\rangle$ denotes time averaging and $\langle \epsilon \rangle$ is the turbulent kinetic energy dissipation rate (here referred to as dissipation). $I_q$ is the non-stationary term equivalent to the first term on the left-hand side of (1.1), which

is given by

$$I_q \equiv -\frac{U}{r^2}\int_0^r s^2 \frac{\partial}{\partial x}\langle(\delta q)^2\rangle \, \mathrm{d}s, \tag{1.4}$$

where $U$ is the mean flow velocity and $s$ is a dummy variable. The similarity scales admitted by (1.3) are twice the turbulent kinetic energy $\langle q^2\rangle$ ($\equiv \langle u^2\rangle + \langle v^2\rangle + \langle w^2\rangle$) and the Taylor microscale $\lambda$, so that for equilibrium similarity (Antonia *et al.* 2003),

$$\langle(\delta\tilde{q})^2\rangle = f(\tilde{r}), \tag{1.5}$$

$$\langle(\delta\tilde{u})(\delta\tilde{q})^2\rangle = -3^{-1/2}R_\lambda^{-1} g(\tilde{r}), \tag{1.6}$$

where a tilde denotes normalization with $\langle q^2\rangle$ or $\lambda$. We note that the general definitions of $\lambda$ and $R_\lambda$, which avoid the ambiguity that arises from the directional dependence of $\langle u^2\rangle$ and $\langle(\partial u/\partial x)^2\rangle$ (see Fulachier & Antonia 1983), are used here, namely,

$$\lambda^2 = 5\nu\frac{\langle q^2\rangle}{\langle\epsilon\rangle}, \tag{1.7}$$

$$R_\lambda = \frac{\langle q^2\rangle^{1/2}\lambda}{3^{1/2}\nu}. \tag{1.8}$$

The most attractive consequences of equilibrium similarity are that $R_\lambda$ is not required to remain constant throughout the decay and that it does not exclude a possible dependence on initial conditions, even for truly homogeneous and isotropic turbulence. For equilibrium similarity, $m < -1$ is thus possible and the theory can apply at any $R_\lambda$. Therefore, experimental and numerical results found in the literature would appear to be consistent with equilibrium similarity. Indeed, some support for the theory was drawn from previous experimental and numerical studies, although George *et al.* (2001) emphasized the need for more detailed experiments to test the theory adequately.

An alternative phenomenological picture was presented by Speziale & Bernard (1992), which could also explain the results of experiments and simulations at finite Reynolds numbers. Their analysis, based on a one-point formulation of the complete self-preserving form of the governing equations, yielded a universal asymptotic solution as $t \to \infty$ with $m = -1$, consistent with Dryden's (1943) theory. They explain the experimentally determined values of $m$ (i.e. $m < -1$) by the limited number of eddy turnover times spanned by experiments and the use of measurements in the region before the asymptotic state has been reached.

Although grid turbulence has been studied extensively since Batchelor & Townsend (1947) and Comte-Bellot & Corrsin (1966), the above discussion shows that many aspects of this flow remain unclear, particularly the observed variations in $m$, and that new experiments are required to clarify these issues. The main focus of this study is on grid-generated turbulence at low to moderate Reynolds numbers (i.e. $20 < R_\lambda < 70$). In particular, we look at the impact of the large-scale anisotropy and how it can be minimized in § 3, the character and evolution of the velocity structure functions in the context of the large-scale organization and the validity of equilibrium similarity in § 4, and the decay of the turbulence with respect to the power-law is discussed in § 5. The primary motivation for the use of low $R_\lambda$ relates to the expectation that the impact of initial conditions should be more easily identifiable at low Reynolds numbers and that equilibrium similarity is postulated to hold at such values. Furthermore, a noteworthy advantage is that, for these flow conditions, the probe resolution relative to the smallest (Kolmogorov) scales of the turbulence is tolerable. An important

| | Grid | Bar shape | $M$ (mm) | $d$ (mm) | $\sigma$ | $R_M$ | $\eta$ (mm) | $\Delta x^*$ | $\Delta y^*$ | $\Delta z^*$ |
|---|---|---|---|---|---|---|---|---|---|---|
| □ | $Sq35$ | Square | 24.76 | 4.76 | 0.35 | 10 400 | 0.21–0.49 | 1.3–1.9 | 2.0–4.8 | 3.2–7.6 |
| ○ | $Rd35$ | Round | 24.76 | 4.76 | 0.35 | 10 400 | 0.24–0.58 | 1.4–1.9 | 1.7–4.2 | 2.8–6.7 |
| ⊗ | $Rd35b$ | Round | 24.76 | 4.76 | 0.35 | 19 700 | 0.15–0.36 | 2.1–3.2 | 2.8–6.7 | 4.4–10 |
| ◇ | $Rd44$ | Round | 24.76 | 6.35 | 0.44 | 10 400 | 0.23–0.54 | 1.2–2.1 | 1.8–4.3 | 3.0–7.0 |
| △ | $Rd44w$ | Round | 24.76 | 6.35 | 0.44 | 10 400 | 0.23–0.56 | 1.2–2.0 | 1.8–4.3 | 2.8–7.0 |

TABLE 1. Details of the grid geometries and experimental conditions of decay experiments.

contribution of the present experiments, the details of which are given in § 2, is that the decay of the turbulence is measured in much greater detail than has been reported previously. In particular, much finer streamwise separations are used between measuring locations to provide five to ten times the number of points typically used in the literature to fit the power law. Furthermore, advancements made over the past four decades in hot-wire anemometry, computer technology, and data acquisition and analysis techniques are used to improve the accuracy relative to previous results. The present measurements, in combination with an improved curve-fitting procedure, improve significantly the reliability of the experimentally determined values for the power-law exponent.

## 2. Experimental procedures

Approximately homogeneous and isotropic turbulence was generated by uniform grids of various geometries. Four square-mesh biplane grids, all with the same mesh size $M = 24.76$ mm, were used to generate different initial conditions. The geometric details of the grids are given in table 1, where $\sigma \equiv d/M\,(2 - d/M)$ is the grid solidity, and general schematics of the grids are shown in figure 1. The geometry of the square-mesh grids was varied by changing the shape (square or round) and diameter $d$ of the bars. In addition, a small helical wire (diameter $d_{wd} = 0.8$ mm) was wound around the bars of $Rd44$ at a pitch of one mesh length ($Rd44w$). The motivation for the design of $Rd44w$ was to reduce the intensity of the dominant frequency observed by Lavoie *et al.* (2005) behind $Rd44$ by reducing the strength of the vortex streets behind the bars of the grid.

An important limitation of grid turbulence is that it inevitably involves a certain degree of anisotropy. In conventional working sections, $\langle u^2 \rangle$ is typically 20–50% larger than $\langle v^2 \rangle$ and $\langle w^2 \rangle$ (e.g. Kistler & Vrebalovich 1966; Uberoi & Wallis 1967). To address this, two working sections, with and without a secondary contraction (WS-A and WS-B, respectively), are used downstream of the grids. Schematics of the wind tunnel and working sections are shown in figure 2. The secondary contraction, which had an area ratio $c = 1.36$ chosen on the basis of the data of Uberoi (1956) and Comte-Bellot & Corrsin (1966), and was located $11M$ downstream of the grids. Because the different turbulence intensities generated by the grids affect the growth rate of the boundary layers at the walls, the floor of each working section was carefully adjusted for each experiment to provide a zero pressure gradient (resulting streamwise variations in $U$ were less than $\pm 0.4\%$).

For grid-generated turbulence, the turbulence kinetic energy decays in space. Taylor's frozen-flow hypothesis allows the time of decay in this case to be associated with the time required for the turbulence to be convected downstream by the mean

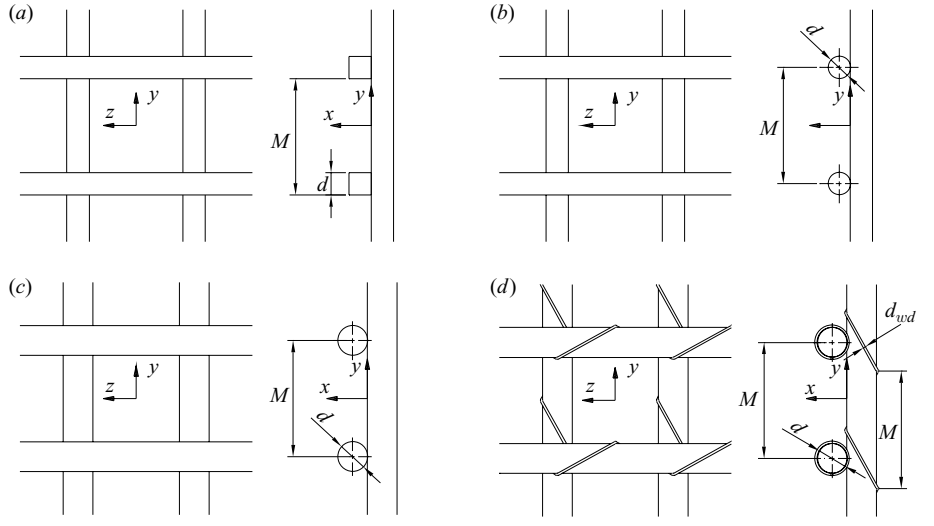


FIGURE 1. Schematic of grid geometries. Dimensions are given in table 1, and $d_{wd} = 0.8$ mm. (*a*) *Sq*35; (*b*) *Rd*35; (*c*) *Rd*44; (*d*) *Rd*44*w*.

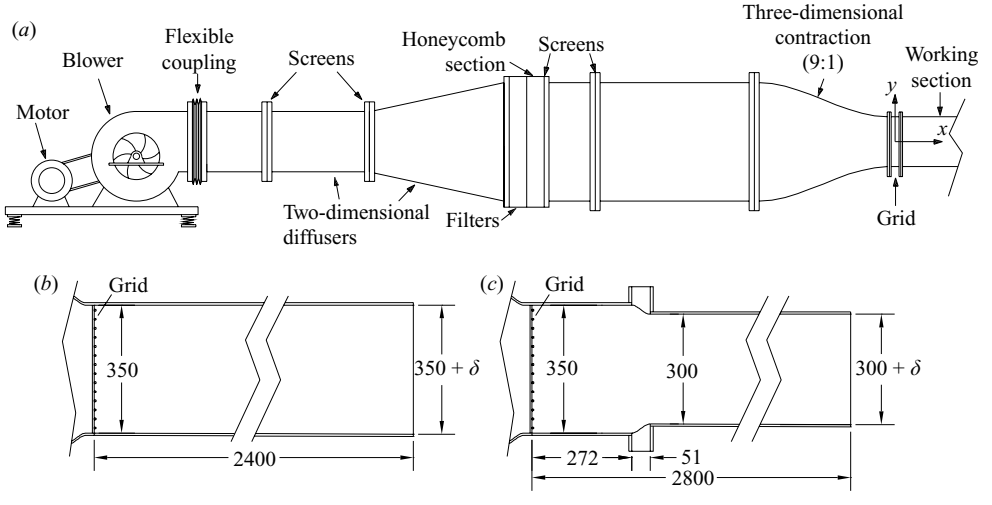


FIGURE 2. Schematic of the wind tunnel and working sections: (*b*) WS-A and (*c*) WS-B. $\delta$ is a small displacement required to achieve a zero pressure gradient along the working sections. All dimensions in mm.

flow. The use of Taylor's hypothesis is warranted in grid turbulence, given the low turbulence intensity and negligibly small streamwise gradients (see Corrsin 1963). Since the velocity is constant in a straight duct section, $x$ remains proportional to time throughout the length of the tunnel. However, the velocity is not constant in WS-B because of the secondary contraction. It is thus more appropriate to define $t$, the time required for the turbulence to be convected from the grid to the downstream location $x$, as (see also Comte-Bellot & Corrsin 1966)

$$t = \int_0^x \frac{\mathrm{d}s}{U(s)}. \tag{2.1}$$

This time is then normalized by $U_0$, the velocity immediately upstream of the grid, and $M$. The use of the convection time instead of the streamwise location allows for a direct comparison of the results between the two working sections.

Two types of experiment were performed. In the first, measurements of the turbulence decay were made for the four biplane grids along the centreline of the tunnel for $20 \leqslant U_0 t/M \leqslant 80$ in WS-A and $25 \lesssim U_0 t/M \lesssim 77$ ($30 \leqslant x/M \leqslant 100$) in WS-B. Measurements were taken at every mesh length along the working sections. A mean velocity $U_0 = 6.4$ m s$^{-1}$ was used and yielded $R_M = U_0 M/\nu \approx 10\,400$ for all grids. Since the various grid geometries produce different turbulence intensities, $R_\lambda$ also varies depending on the grid (e.g. Lavoie *et al.* 2005). Therefore, measurements were also obtained for $Rd35$ with $R_M \simeq 19\,700$ (or $U_0 \simeq 12.1$ m s$^{-1}$) to reproduce equivalent values of $R_\lambda$ as those found for $Sq35$ at $R_M \simeq 10\,400$. For the second type of experiment, measurements were taken at a constant downstream location with different $U_0$. The measuring locations were $U_0 t/M = 60$ for WS-A and $U_0 t/M \simeq 62$ ($x/M = 80$) for WS-B.

The energy dissipation rate can be estimated indirectly and reliably from the turbulent kinetic energy budget. In the context of spatially decaying grid turbulence, the energy budget can be expressed as (e.g. Tennekes & Lumley 1972)

$$\langle \epsilon \rangle_d = -\frac{U}{2} \frac{\mathrm{d}\langle q^2 \rangle}{\mathrm{d}x}, \tag{2.2}$$

where the subscript $d$ is used to indicate that $\langle \epsilon \rangle$ is obtained from the decay of $\langle q^2 \rangle$. While this method can be used to estimate $\langle \epsilon \rangle$ for the decay measurements described above, it is obtained from the similarity form of (1.3) for the single-location experiments. By substituting (1.5) and (1.6) into (1.3), the transport equation can be rewritten as

$$g + 2f' - [5\Gamma_1/m - 10\Gamma_2]\,\tilde{r}^{-2} = (20/3)\,\tilde{r}\ , \tag{2.3}$$

where the prime indicates differentiation with respect to $\tilde{r}$, while $\Gamma_1 \equiv \int_0^{\tilde{r}} \tilde{s}^3 f' \,\mathrm{d}\tilde{s}$ and $\Gamma_2 \equiv \int_0^{\tilde{r}} \tilde{s}^2 f \,\mathrm{d}\tilde{s}$. Lavoie *et al.* (2005) have shown that (2.3) is verified approximately at all scales (see also figure 3) so that adequate estimates of $\langle \epsilon \rangle$ can be obtained, as is demonstrated below. The dissipation rate obtained with this method is denoted by the subscript $sb$ (for scale-by-scale budget) and is taken as the value of $\langle \epsilon \rangle$ that balances (2.3) at $\tilde{r} = 1$ with the measured distributions for $\langle (\delta q)^2 \rangle$ and $\langle (\delta u)(\delta q)^2 \rangle$. The selection of $\tilde{r} = 1$ is based on the observation that (2.3) is nearly perfectly balanced at this location. The estimate $\langle \epsilon \rangle_{sb}$ offers the particular advantage that the smallest scales need not be resolved to the same degree as that required if $\langle \epsilon \rangle$ were obtained from the velocity derivative statistics, e.g. $\langle \epsilon \rangle_{iso} = 15\nu \langle (\partial u/\partial x)^2 \rangle$. A similar approach has been used by Kang, Chester & Meneveau (2003) based on the transport equation for $\langle (\delta u)^2 \rangle$, although it relied on Kolmogorov's second similarity hypothesis (i.e. $\langle (\delta u)^2 \rangle \sim \langle \epsilon \rangle^{2/3} r^{2/3}$) and the $k$–$\epsilon$ model to estimate the non-stationary term. Figure 4 compares the ratio $\langle \epsilon \rangle_{sb}/\langle \epsilon \rangle_d$ for some of the grids in both working sections. Even for $Rd44$, for which equilibrium similarity is the least accurate (Lavoie *et al.* 2005, see also § 4.2), the difference between $\langle \epsilon \rangle_d$ and $\langle \epsilon \rangle_{sb}$ remains typically within $\pm 10\%$. Also included in figure 4 are error bars on the estimate of $\langle \epsilon \rangle_{sb}$ for $Sq35$, which illustrate the insensitivity of $\langle \epsilon \rangle_{sb}$ to uncertainties in $m$. These error bars represent an uncertainty of $\pm 15\%$ on $m$, a grossly conservative estimate, which only translates to an error of 3–4% in $\langle \epsilon \rangle_{sb}$.

A one-component vorticity probe (figure 5) consisting of two parallel wires and an X-wire was used to measure the turbulence behind the grids. The dimensions of

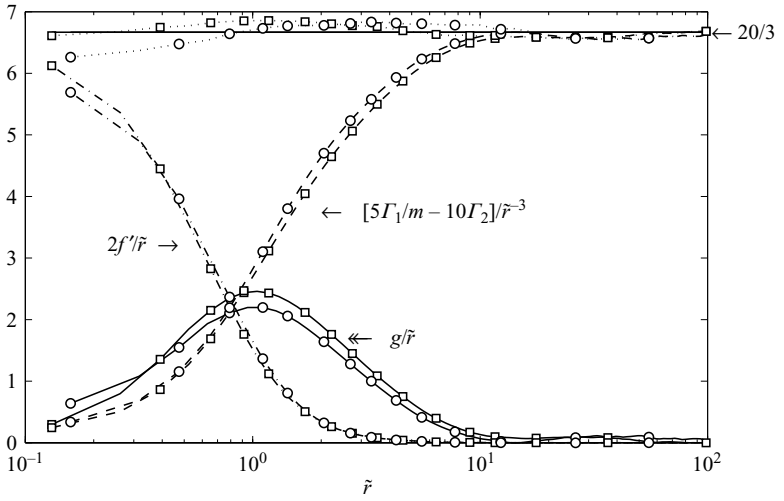


FIGURE 3. Examples of the scale-by-scale budget described by (2.3) and compensated with $r$ for $Rd35$ (○) in WS-A at $U_0t/M = 60$ and $Sq35$ (□) in WS-B at $U_0t/M \simeq 47$. The sum of the left-hand side of (2.3) is represented by the dotted line.

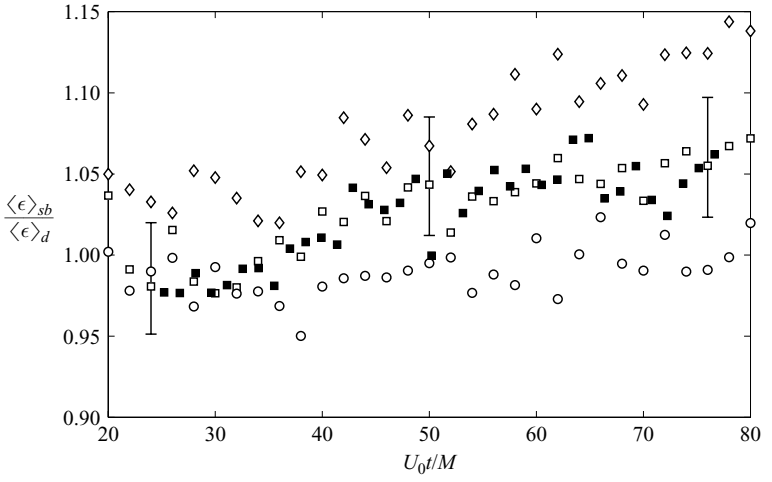


FIGURE 4. Ratio $\langle\epsilon\rangle_{sb}/\langle\epsilon\rangle_d$ for $Sq35$ (□), $Rd35$ (○) and $Rd44$ (◇) in WS-A (open symbol) and WS-B (filled symbols). Here and in the subsequent figures, only every second point is shown to avoid crowding.

the probe are compared in table 1 to the values for the Kolmogorov length scale $\eta\,(\equiv \nu^{3/4}/\langle\epsilon\rangle^{1/4})$ in both working sections. The asterisk denotes normalization with $\eta$, while $\Delta x = U/f_s$, where $f_s$ is the sampling frequency. Since $\eta$ grows during the decay, the resolution of the probe improves as $U_0t/M$ increases. The dimensions of the probe were chosen to meet the minimum separation criteria at $U_0t/M = 80$ for X- and parallel-wires, as outlined by Zhu & Antonia (1995) and Zhou *et al.* (2003) to minimize errors due to wire interference and noise contamination. The spectral correction equations for the X-wire and one-component vorticity probes outlined by Zhu & Antonia (1996) were used to correct the measured values of the variance of

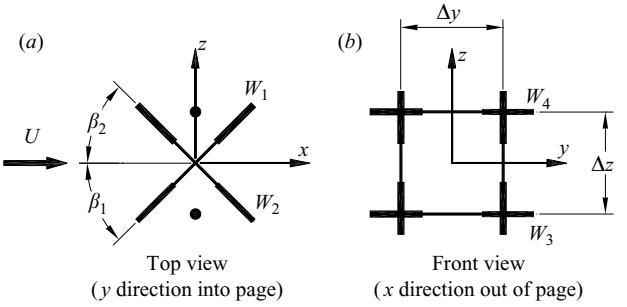


FIGURE 5. One-component vorticity probe. $\Delta y \simeq 1.0$ mm, $\Delta z \simeq 1.6$ mm, $\beta_1 \simeq \beta_2 \simeq 45°$. All wires have a diameter of 2.5 μm and are etched from Wollaston (Pt–10% Rh) material to a length of approximately 0.5 mm. (*a*) Top view (*y*-direction into page); (*b*) front view (*x*-direction out of page).

the velocity and velocity derivative fluctuations for bias errors related to the limited probe resolution.

The wires were operated with in-house constant temperature circuits at an overheat ratio of 1.5. The signals were amplified and low-pass filtered at a cutoff frequency $f_c$, which was selected to correspond to the onset of electronic noise, and varied depending on the grid, flow velocity and measurement location. The signals were sampled at a frequency $f_s \geqslant 2f_c$ and digitized with a 16 bit A/D converter. The record duration for the turbulence decay experiments was optimized to yield a statistical convergence of $\langle q^2 \rangle$ to within $\pm 1\%$ at each measuring station and $\pm 5\%$ on the negative peak value of $\langle (\delta u)(\delta q)^2 \rangle$. The latter criterion was only met every 10 mesh lengths since it required particularly long records (as long as 6 min at $x/M = 80$). The sampling time for the single-point measurements met both criteria. The statistical convergence of a given quantity was determined from the precision index of that quantity and the number of independent samples obtained (see Benedict & Gould 1996).

The X-wire was calibrated using a look-up table, as described by Burattini & Antonia (2005), with calibration angles at 2.5° intervals. The single wires were calibrated with standard velocity calibrations to which third-order polynomials were fitted. Seven to eight calibration velocities were used for both X- and single-wires. Since the flow is axisymmetric for this configuration (see Lavoie *et al.* 2005), the $v$ and $w$ statistics are assumed equal for the remainder of this paper. The $w$ and mixed $u$–$w$ statistics were derived from the X-wire, while the statistics of $u$ were obtained from the average of the single wires since they provide a more accurate measurement of $u$ than the X-wire.

## 3. Isotropy of velocity and vorticity fluctuations

It is common to assess the isotropy of the energy-containing scales from the ratio $\langle u^2 \rangle / \langle w^2 \rangle$ ($\equiv K$), which is shown in figure 6 for the different grids used in both working sections. The data for $Rd35b$ are not included to minimize crowding since these are nearly identical to the other round-rod grids. For WS-A, $K$ remains nearly constant with $U_0 t/M$ for all grids. There are, however, some noticeable variations for $U_0 t/M < 30$ for the round-rod grids; this reflects a slower development of the turbulence behind these grids. We remark that $K$ for the round-rod grids does not show a significant dependence on $\sigma$ or $R_M$ (the scatter is within the measurement uncertainty and repeatability of the experiments). Experiments performed close to the

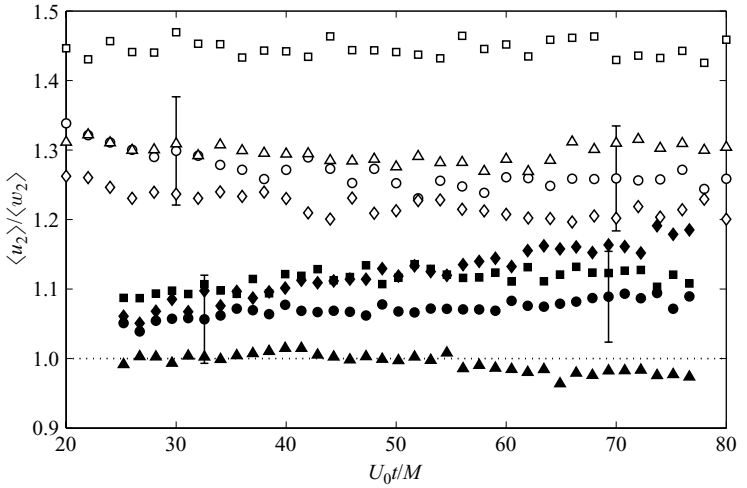


FIGURE 6. Evolution of the isotropic parameter $K$ behind grids in WS-A (open symbols) and WS-B (filled symbols). $Sq35$ (□), $Rd35$ (○), $Rd44$ (◇) and $Rd44w$ (△). The isotropic value of 1 is marked by the dotted line and error bars are shown for $Rd35$.

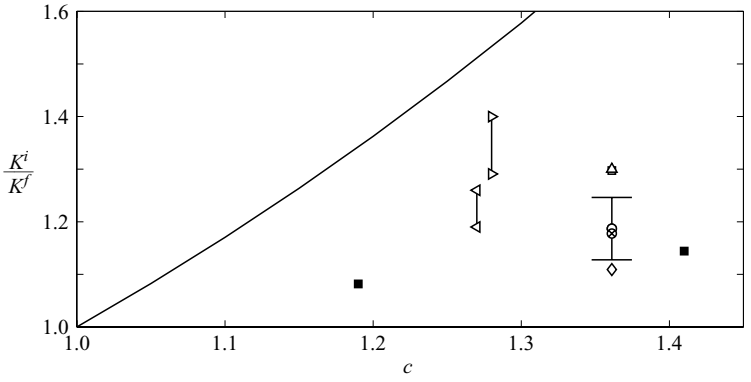


FIGURE 7. Effect of secondary contraction ($c$ is the area ratio for the contraction) on isotropy. $Sq35$ (□), $Rd35$ (○), $Rd35b$ (⊗), $Rd44$ (◇), $Rd44w$ (△), and data from Comte-Bellot & Corrsin (1966) (◁), Uberoi & Wallis (1966) (▷) and Bennett & Corrsin (1978) (■). The solid line represents the predictions from Batchelor (1953), and the error bar for $Rd35$ is included.

grids (Lavoie, Djenidi & Antonia 2006) suggest that the phenomenology responsible for the larger anisotropy for $Sq35$ in WS-A, compared to the round-rod grids, is related to differences in the interaction of the wakes in the region immediately downstream of each grid. As expected, the turbulence is more closely isotropic downstream of the contraction, while it is relevant to highlight that $Rd44w$ yields nearly perfect isotropy.

The ratio of the values of $K$ before and after the contraction (subscripts $i$ and $f$, respectively) for the present experiments are compared to other published results in figure 7. Batchelor's predictions on the effect of a sudden axisymmetric contraction on HIT are also included in the figure as a reference (see Batchelor 1953, pp. 68–75). It is expected that these predictions will overestimate the effect of the contraction since it is not sudden enough for viscous, and more importantly, inertial effects to be neglected (indeed, most contractions are not sudden enough because of practical

considerations). We note that the uncertainty of this ratio is illustrated by the error bar for $Rd35$ and also by the range of values spanned by the data of Comte-Bellot & Corrsin (1966) and Uberoi & Wallis (1966). For the present range of Reynolds numbers, the impact of the contraction on $K$ does not vary with $R_\lambda$ for a given grid. Notwithstanding some scatter in the data, the amelioration in $K$ shows some dependence on grid geometry. As a result of this dependence, and since the grids do not produce the same degree of anisotropy, different contraction ratios would be required to produce $K = 1$ for all cases.

The velocity derivative and vorticity statistics are more representative of the small-scale motions than the parameter $K$. For locally isotropic turbulence,

$$\left\langle \left(\frac{\partial u}{\partial z}\right)^2 \right\rangle = 2\left\langle \left(\frac{\partial u}{\partial x}\right)^2 \right\rangle, \tag{3.1a}$$

$$\left\langle \left(\frac{\partial w}{\partial x}\right)^2 \right\rangle = 2\left\langle \left(\frac{\partial u}{\partial x}\right)^2 \right\rangle, \tag{3.1b}$$

$$\left\langle \left(\frac{\partial u}{\partial z}\right)\left(\frac{\partial w}{\partial x}\right) \right\rangle = -\frac{1}{2}\left\langle \left(\frac{\partial u}{\partial x}\right)^2 \right\rangle, \tag{3.1c}$$

$$\langle \omega_y^2 \rangle = 5\left\langle \left(\frac{\partial u}{\partial x}\right)^2 \right\rangle. \tag{3.1d}$$

A formal distinction is made between local homogeneity and isotropy, where the assumptions of homogeneity and isotropy apply only for the small scales, and the condition of homogeneity and isotropy that relates to the overall flow. Relations (3.1$a$)–(3.1$c$) are shown in figure 8 for $Sq35$, $Rd44$ and $Rd44w$, while figure 9 displays (3.1$d$) for the different grids. Also included in figure 8($a$) are the data of Tsinober, Kit & Dracos (1992), Mydlarski & Warhaft (1996) and Antonia, Zhou & Zhu (1998).

The deviations from isotropy of $\langle(\partial u/\partial z)^2\rangle$ and $\langle(\partial w/\partial x)^2\rangle$ in WS-A are similar to those previously reported under comparable flow conditions (figure 8a). Nonetheless, $\langle\omega_y^2\rangle$ satisfies isotropy to a close approximation (figure 9), as was also found by Antonia *et al.* (1998). This is to be expected since $\langle(\partial u/\partial z)(\partial w/\partial x)\rangle$ is nearly isotropic and the small departure from local isotropy causes opposite deviations for (3.1$a$) and (3.1$b$). The secondary contraction yields good isotropy for $\langle(\partial u/\partial z)^2\rangle$ (figure 8$b$), while $\langle(\partial w/\partial x)^2\rangle$ retains a similar deviation from (3.1$b$).

The approach used above to assess the level of isotropy is limited since ratios such as $K$ and $\langle(\partial w/\partial x)^2\rangle/\langle(\partial u/\partial x)^2\rangle$ are representative of a range of scales. A more local description of the scales affected by the anisotropy of the flow is provided in figure 10. Here, the measured distribution of $\langle(\delta w)^2\rangle$ is compared to that calculated (denoted by the subscript $cal$) with the isotropic relation (e.g. Monin & Yaglom 1975)

$$\langle(\delta w)^2\rangle_{cal} = \frac{r}{2}\frac{\mathrm{d}\langle(\delta u)^2\rangle}{\mathrm{d}r} + \langle(\delta u)^2\rangle, \tag{3.2}$$

where the measured distribution of $\langle(\delta u)^2\rangle$ was used as input. The ratio $\tilde{W}_T$, where $W_T$ is the width of the tunnel, is included as an indication of the values of $\tilde{r}$ that may be affected by the size of the tunnel. Also indicated in the figure are the separations that correspond to the integral length scale $\tilde{L}_q \equiv \int_0^{\tilde{r}_0} \tilde{B}_{q,q}(\tilde{r})\,\mathrm{d}\tilde{r}$, where $r_0$ is the first zero-crossing of $B_{q,q}(r) \equiv B_{u,u}(r) + B_{v,v}(r) + B_{w,w}(r)$. Since $\tilde{L}_q$ is slightly different for each grid, this ratio corresponds to a short range of $\tilde{r}$ in figure 10. The ratio $\langle(\delta w)^2\rangle_{cal}/\langle(\delta w)^2\rangle$ is constant and close to one at small separations for both

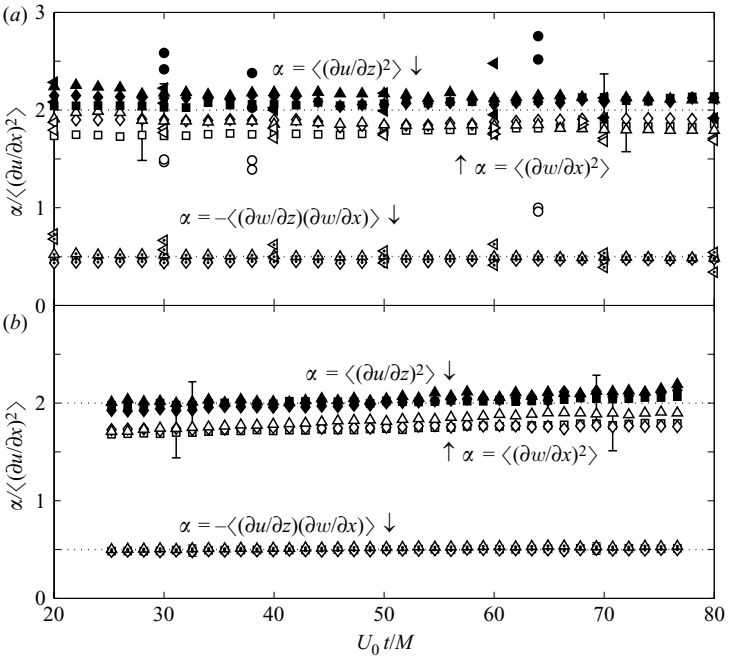


FIGURE 8. Ratio of second-order velocity derivative moments for $Sq35$ (□), $Rd44$ (◇) and $Rd44w$ (△). (*a*) WS-A; (*b*) WS-B. Also included in (*a*): ○, from Tsinober *et al.* (1992); ▷, from Mydlarski & Warhaft (1996); ◁, Antonia *et al.* (1998). $\alpha = \langle(\partial w/\partial x)^2\rangle$ (open symbols), $\langle(\partial u/\partial z)^2\rangle$ (filled symbols) and $-\langle(\partial u/\partial z)(\partial w/\partial x)\rangle$ (symbols with dots). Isotropic values, 2 for the former two ratios and 0.5 for the latter, are indicated by dotted lines. Error bars shown for $Sq35$.

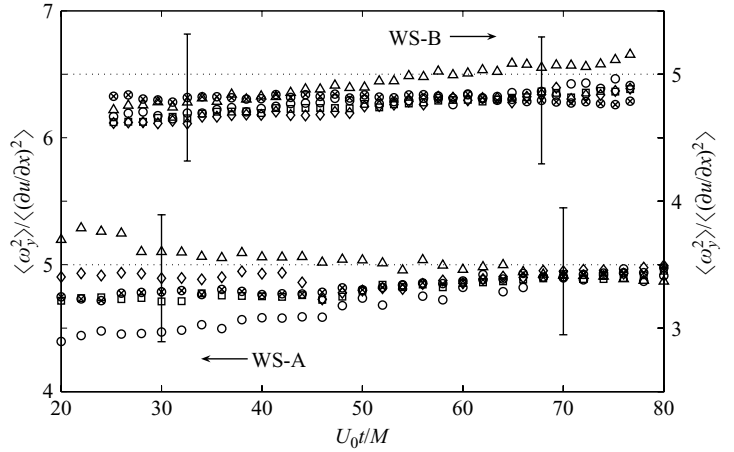


FIGURE 9. Streamwise evolution of $\langle\omega_y^2\rangle/\langle(\partial u/\partial x)^2\rangle$ in WS-A (left-hand axis) and WS-B (right-hand axis). $Sq35$ (□), $Rd35$ (○), $Rd35b$ (⊗), $Rd44$ (◇) and $Rd44w$(△). Isotropic value marked with dotted lines. Error bars shown for $Rd44$ (WS-A) and $Rd35b$ (WS-B).

working sections. The small departure from the isotropic value of one at small $\tilde{r}$ is related to the deviations of (3.1*b*) from isotropy (figure 8), since it can be shown that $\lim_{r\to 0} \mathrm{d}\langle(\delta\alpha)^2\rangle/\mathrm{d}r = 2\langle(\partial\alpha/\partial x)^2\rangle r$ (e.g. Danaila *et al.* 2002). Because of the anisotropy present in WS-A, the ratio $\langle(\delta w)^2\rangle_{cal}/\langle(\delta w)^2\rangle$ increases for separations of the order

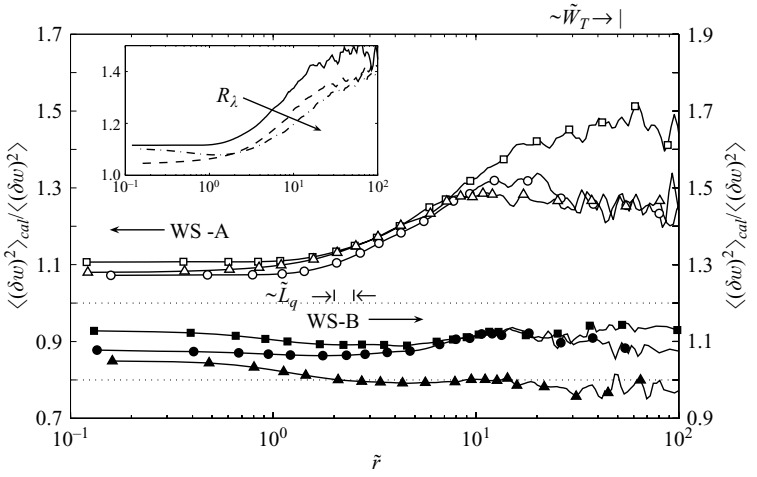


FIGURE 10. Ratio of calculated (subscript *cal*) and measured distributions of $\langle(\delta w)^2\rangle$ in WS-A (open symbols) and WS-B (closed symbols). $Sq35$ (□), $Rd35$ (○) and $Rd44w$ (△). Isotropic values are marked by dotted lines. The inset illustrates the dependence of this ratio on $R_\lambda$ for $Sq35$ in WS-A; $R_\lambda$ *simeq* 43 (——), 51 (— — —) and 66 (— · —).

of $L_q$ and higher. The improved isotropy at the large scales, owing to the secondary contraction, yields nearly constant values close to 1 at all separations in WS-B, as expected. The effect of $R_\lambda$ on $\langle(\delta w)^2\rangle_{cal}/\langle(\delta w)^2\rangle$ in WS-A is illustrated for $Sq35$ in the inset of figure 10. As $R_\lambda$ increases, the smallest values of $\tilde{r}$ affected by the anisotropy also increase, but remain roughly equal to $\tilde{L}_q$. The results of figure 10 thus illustrate that the anisotropy is mainly restricted to the large scales of the flow.

An important observation from figures 8–10 is that the grid geometry, with or without the secondary contraction, has no clear effect on the isotropy of the small scales in decaying grid turbulence. (Although there is a notable reduction in the scatter of the data between grids in figures 8 and 9 for WS-B, this is within measurement uncertainty.) This indicates that the anisotropic strain rate applied by the secondary contraction, which is expected to disturb local isotropy in the contraction and shortly thereafter (as shown experimentally by Uberoi 1956), does not have a persistent effect on small-scale isotropy for the downstream locations investigated. Furthermore, these results imply that the large-scale anisotropy is effectively damped by the energy cascade, consistent with the postulate of local isotropy of Kolmogorov (1941). Thus, for this particular flow, the directional information at the large scales ($r > L_q$) does not significantly affect isotropy at the small scales. In previous studies of grid turbulence, the small imbalance of (3.1*b*) was typically attributed to the large-scale anisotropy. However, the present results do not support this belief since the imbalance remains even when isotropy at the large scales is significantly improved. To the best of our knowledge, the anisotropy of $\langle(\partial w/\partial x)^2\rangle$ is consistently observed in grid turbulence measured with multi-sensor hot-wire probes (e.g. Tsinober *et al.* 1992; Mydlarski & Warhaft 1996; Antonia *et al.* 1998). On the other hand, the measurements of Michelet *et al.* (1998), made via laser-Doppler anemometry, appear to satisfy (3.1*b*), although their results contain significant scatter. This observation would suggest that the measured anisotropy could be due to errors associated with the hot-wire measurements and not necessarily a characteristic of grid turbulence. This point, however, requires further investigation and is not considered here.

| | WS-A | | | | | | WS-B | | | | | |
|---|---|---|---|---|---|---|---|---|---|---|---|---|
| Grid | $U_0t/M$ | $U_0$ (m s$^{-1}$) | $\langle\epsilon\rangle$ | $R_\lambda$ | $\lambda$ (mm) | $\eta$ (mm) | $U_0t/M$ | $U_0$ (m s$^{-1}$) | $\langle\epsilon\rangle$ | $R_\lambda$ | $\lambda$ (mm) | $\eta$ (mm) |
| $Sq35$ | 60 | 6.4 | $\langle\epsilon\rangle_d$ | 43 | 5.3 | 0.41 | 80 | 6.4 | $\langle\epsilon\rangle_d$ | 40 | 5.3 | 0.42 |
| $Rd35$ | 40 | 12.1 | $\langle\epsilon\rangle_d$ | 42 | 4.5 | 0.35 | 80 | 12.2 | $\langle\epsilon\rangle_d$ | 39 | 3.8 | 0.31 |
| $Rd44$ | 60 | 9.8 | $\langle\epsilon\rangle_{sb}$ | 40 | 4.1 | 0.33 | 40 | 6.4 | $\langle\epsilon\rangle_d$ | 36 | 3.7 | 0.31 |
| $Rd44w$ | 54 | 9.7 | $\langle\epsilon\rangle_{sb}$ | 39 | 3.9 | 0.31 | 80 | 10.2 | $\langle\epsilon\rangle_{sb}$ | 40 | 4.0 | 0.32 |

TABLE 2. Basic turbulence quantities for experimental results of § 4.1 (figure 11). Also indicated is the method used to estimate $\langle\epsilon\rangle$.

## 4. Second- and third-order structure functions

### 4.1. *Effects of initial conditions on structure functions*

Lavoie *et al.* (2005) have reported that the shape of the bars used to build the grid can have a significant effect on scales of the order of $\lambda$ for a constant $R_M \simeq 10\,400$. However, the value of $R_\lambda$ for the three grids used varies by as much as 45%. In order to isolate the effect of initial conditions from those related to changes in $R_\lambda$, the focus here is on measurements obtained for a constant $R_\lambda$. Details of the experimental conditions for the data presented in this section are given in table 2.

The second- and third-order structure functions measured for the different grids in WS-A and WS-B are shown normalized with $\langle q^2\rangle$ and $\lambda$ in figure 11. We note that separations of the order of the tunnel width are well within the region where the second- and third-order function reach their respective asymptotic values for $r \to \infty$. The turbulence is therefore not expected to have been affected by the finite width of the tunnel, which is typically equal to 20–30$L_q$. In either working section, there are negligible differences in $\langle(\delta\tilde{q})^2\rangle$ and $\langle(\delta\tilde{u})(\delta\tilde{q})^2\rangle$ owing to grid geometry for $\tilde{r} < 4$. This shows that the differences in $\langle(\delta\tilde{q})^2\rangle$ observed by Lavoie *et al.* (2005) for $\tilde{r} \simeq 1$ are primarily due to changes in $R_\lambda$. In WS-A, the grid geometry has an important influence on the large scales of the flow, as is illustrated by the variations in the shapes of $\langle(\delta\tilde{q})^2\rangle$ and $\langle(\delta\tilde{u})(\delta\tilde{q})^2\rangle$ between the various grids for $\tilde{r} > 4$. In particular, $\langle(\delta\tilde{q})^2\rangle$ approaches the value of 2 monotonically from below for $Sq35$, whereas it overshoots at large separation ($\tilde{r} \approx 13$) for the round-rod grids. This overshoot is due to the more periodic nature of the large scales generated by the round-rod grids, particularly for $Rd44$, compared to $Sq35$. The geometry of the grid has a persistent influence on the character of the turbulence in the streamwise direction for the whole region spanned by the present experiments.

The more periodic character of the turbulence behind the round-rod grids is more readily ascertained from figure 12, where the one-dimensional spectra of the transverse velocity $\phi_w(k_1)$ measured behind the grids are shown. The Strouhal number ($St \equiv k_1 d/2\pi$) of the sharp peak in the spectra, which is associated with strong periodic motion in the flow, is independent of $x$ and is roughly located at the wavenumber $k_1 \simeq (cM)^{-1}$. The disappearance of the sharp peak in the spectra for $Rd44w$ compared to $Rd44$ in figures 12(*b*) and 12(*d*) shows that the helical wire effectively reduces the importance of the periodicity behind the latter grid, as expected. The strain rate applied on the flow by the secondary contraction causes the significant periodic motion produced by $Rd35$ and $Rd35b$ to break down (figure 12*c*).

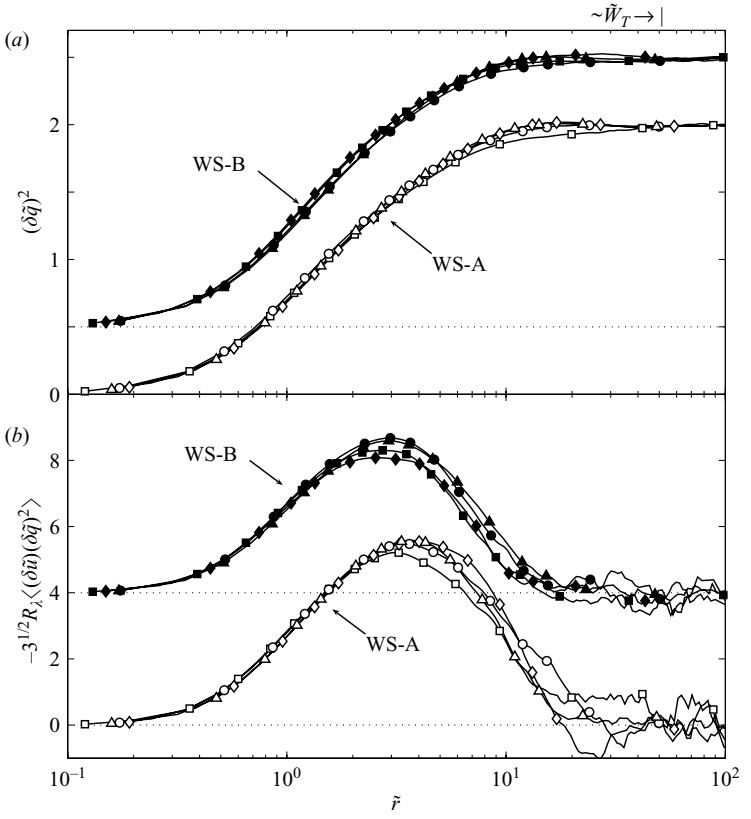


FIGURE 11. Distributions of the second- and third-order structure functions for $Sq35$ (□), $Rd35$ (○), $Rd44$ (◇) and $Rd44w$ (△) at $R_\lambda \simeq 40$ in WS-A (open symbols, no offset) and WS-B (filled symbols, with offset: (*a*) 0.5; (*b*) 4).

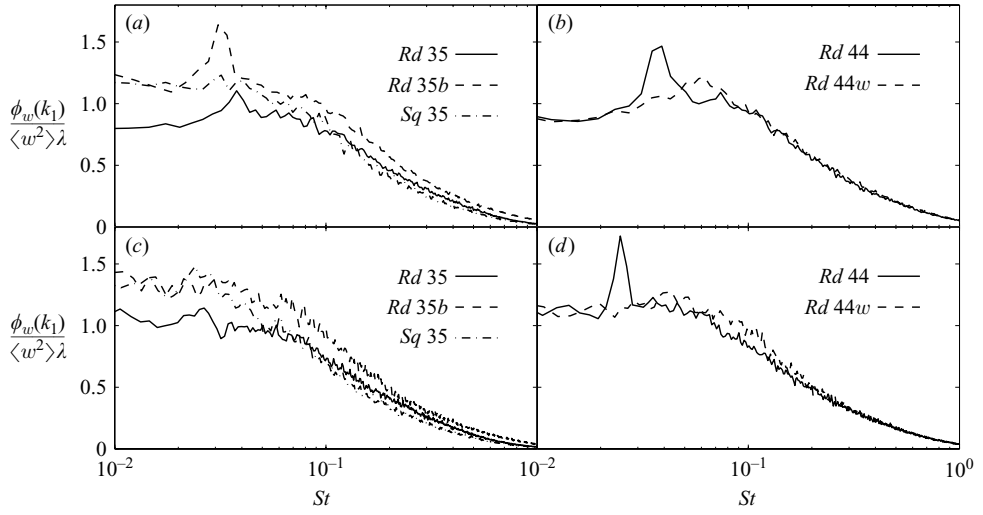


FIGURE 12. (*a*, *b*) WS-A; (*c*, *d*) WS-B. Lateral velocity spectra, defined as $\int_0^\infty \phi_u(k_1)\mathrm{d}k_1 = \langle w^2\rangle$, measured at $U_0t/M = 20$ in WS-A and $U_0t/M = 25$ in WS-B behind all the grids.

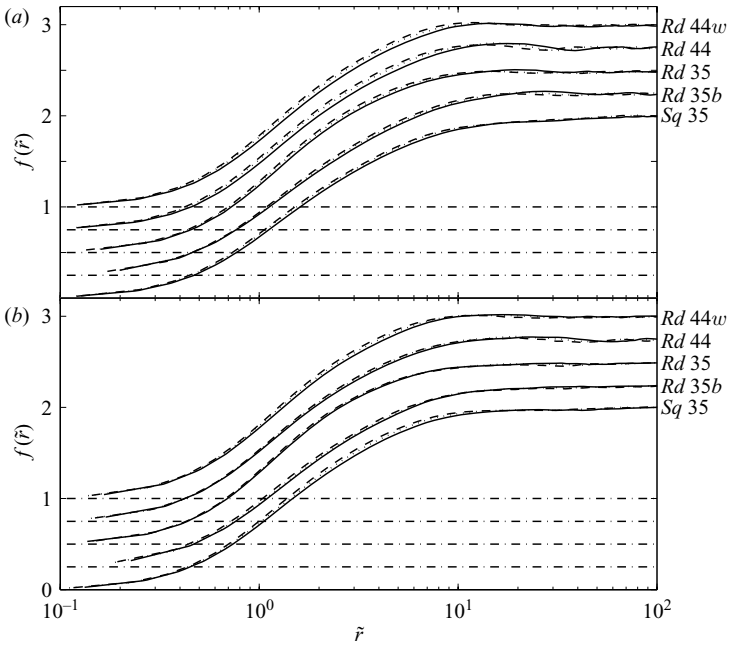


FIGURE 13. Distributions of the second-order structure function normalized with $\langle q^2 \rangle$ and $\lambda$ in WS-A and WS-B. $Sq35$ (no offset), $Rd35b$ (offset 0.25), $Rd35$ (offset 0.5), $Rd44$ (offset 0.75) and $Rd44w$ (offset 1.0). (*a*) WS-A: $U_0 t/m = 40$ (——); 60 (· · ·); 80 (— — —). (*b*) WS-B: $U_0 t/M \simeq 40$ (——); 55 (· · ·); 77 (— — —).

For WS-B, the shapes of $\langle (\delta\tilde{q})^2 \rangle$ and $\langle (\delta\tilde{u})(\delta\tilde{q})^2 \rangle$ are notably more uniform than in WS-A. This would suggest that, in addition to the variations caused by the changes in periodicity, the anisotropy can account for some of the differences in the structure functions measured in WS-A. This point can be further highlighted if we note that the scales most affected by the anisotropy in WS-A (figure 10) are also the scales that display the strongest dependence on initial conditions. This is also supported by the nearly identical distributions of $\langle (\delta\tilde{q})^2 \rangle$ for the round-rod grids in WS-A – recall that they all involved the same level of anisotropy (figure 6).

### 4.2. *Similarity of structure functions*

Distributions of $f(\tilde{r})$ are shown in figure 13 for both working sections. Three locations in the range $40 \leqslant U_0 t/M \leqslant 80$ are shown. In each case, the collapse is adequate, although not complete. The collapse of $f(\tilde{r})$ is assessed in a more quantitative manner in figure 14, where the difference between the distributions measured at two locations is plotted as a function of $\tilde{r}$. The two locations were selected to represent comparable decay times in both working sections. Notwithstanding some variations due to uncertainties, the maximum deviation is generally in the vicinity of $\tilde{r} = 3$, with a peak value between 2 and 5%. For the grids with a strong periodic component in WS-A (i.e. $Rd35$, $Rd35b$ and $Rd44$), there is a negative peak at $\tilde{r} \simeq 25$ with a magnitude comparable to the peak at $\tilde{r} = 3$. This feature is not present for $Sq35$ and $Rd44w$, for which periodicity is not as important. As discussed in § 4.1, the location of the peak in the spectra is constant with $x$. Therefore, the location of the dominant frequency does not remain invariant when scaled with similarity variables since $\lambda$ grows in the streamwise direction. The periodicity associated with this peak in the

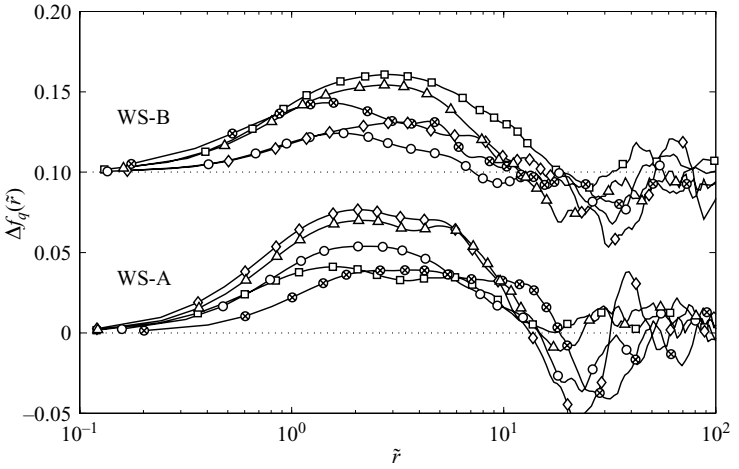


FIGURE 14. Deviation from similarity. $\Delta f_q$ is defined arbitrarily as the difference between $f_q$ at $U_0t/M = 40$ and 80 (WS-A) or $U_0t/M \simeq 37$ and 77 (WS-B). $Sq35$ (□), $Rd35$ (○), $Rd35b$ (⊗), $Rd44$ (◇) and $Rd44w$ (△).

spectra must then result in a deviation from similarity in the structure functions at separations equivalent to the wavenumber of the peak.

Figure 15 shows $\langle(\delta u)(\delta q)^2\rangle$ normalized according to equilibrium similarity. As for the second-order structure function, the collapse is adequate though not perfect. The most important deviations from the similarity hypothesis in WS-A are found for $\tilde{r} > 3$, whereas the collapse of $g(\tilde{r})$ in WS-B is generally better at these scales. Although the results of figures 13–15 suggest that large-scale periodicity and anisotropy tend to accentuate deviations from equilibrium similarity, the overall collapse on similarity is not necessarily improved for the grids where periodicity is reduced and isotropy satisfactory. This is particularly evident in figure 14, where $Rd44w$, the grid that produces the most isotropic turbulence with minimal large-scale periodicity, displays the largest deviations from similarity. We therefore conclude that grid turbulence does not decay following equilibrium similarity.

Antonia & Orlandi (2004) demonstrated that Kolmogorov similarity is more accurate than equilibrium similarity for the small scales where the non-stationary term in the transport equation for $\langle(\delta q)^2\rangle$ is negligible. It can be shown that $I_q$ is not relevant when $r \ll L_q$ or $R_\lambda \to \infty$ (Saffman 1968). For these conditions, (1.3) simplifies to the general form of Kolmogorov's equation (Antonia *et al.* 1997), namely,

$$-\langle(\delta u)(\delta q)^2\rangle + 2\nu\frac{\mathrm{d}}{\mathrm{d}r}\langle(\delta q)^2\rangle = \tfrac{4}{3}\langle\epsilon\rangle r. \tag{4.1}$$

Batchelor (1947) has shown that self-preservation of the structure functions on Kolmogorov variables ($\eta$ and $U_K \equiv \nu^{1/4}\langle\epsilon\rangle^{1/4}$) is satisfied by Kolmogorov's equation. However, this does not coincide with a complete self-preservation of the turbulence unless $R_\lambda \to \infty$ because the non-stationary term is not considered. As noted by George (1992), self-preservation based on Kolmogorov variables is fully consistent with equilibrium similarity for $R_\lambda \to \infty$. For isotropic turbulence (e.g. Tennekes & Lumley 1972), $\lambda^* = 15^{1/4}R_\lambda^{1/2}$ and $\langle q^{*2}\rangle = (3/15^{1/2})R_\lambda$. Therefore, the difference between equilibrium similarity and Kolmogorov normalization increases for experiments where $R_\lambda$ decays, since the relevant scales of the turbulence do not remain proportional to

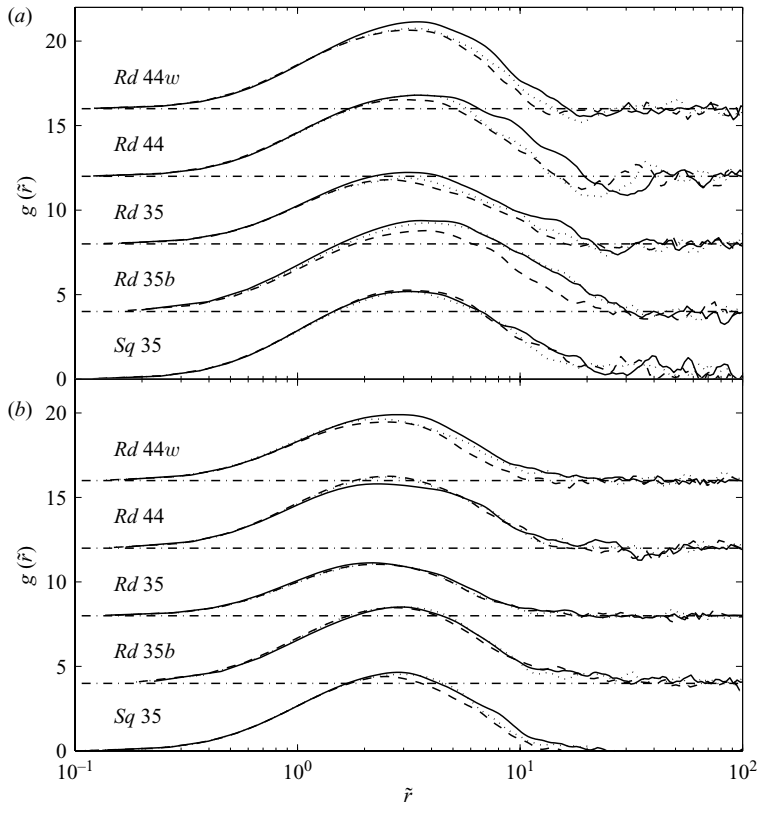


FIGURE 15. Distributions of the third-order structure function normalized according to equilibrium similarity in WS-A and WS-B. *Sq*35 (no offset), *Rd*35*b* (offset 4), *Rd*35 (offset 8), *Rd*44 (offset 12) and *Rd*44*w* (offset 16). (*a*) WS-A: $U_0t/M = 40$ (——); 60 (· · ·); 80 (— — —). (*b*) WS-B: $U_0t/M \simeq 40$ (——); 55 (· · ·); 77 (— — —).

each other. The importance of the $R_\lambda$ decay can be assessed by substituting (1.2), (1.7) and (2.2) into (1.8), then differentiating with respect to time to yield

$$\frac{1}{R_\lambda}\frac{\mathrm{d}R_\lambda}{\mathrm{d}t} = \left[\frac{m+1}{2}\right]\left(\frac{U_0t}{M} - \frac{U_0t_0}{M}\right)^{-1}. \tag{4.2}$$

Hence, the decay of $R_\lambda$ is more significant for values of $m$ much lower than $-1$ (term in square brackets), although its importance decreases with $U_0t/M$ (term in parentheses). Starting from the premise that Kolmogorov normalization is the relevant normalization at small scales, the quality of the collapse based on equilibrium similarity should be best for experiments where $m$ is closest to $-1$. These arguments are consistent with Batchelor's (1948) expectation that complete similarity is only possible for constant $R_\lambda$ (i.e. $m = -1$), and therefore, all turbulent scales remain proportional. The values of $m$ for grid turbulence do not deviate much from $-1$ (typically 10–35%) and the range of decay times spanned by nearly all experiments is fairly short. This is also true for the present experiments, where the number of large-eddy turnover times associated with the region where the turbulence is approximately

homogeneous and isotropic is typically 4–6† and the variation in $R_\lambda$ is less than 15%. These limitations prevent an unambiguous verification of the above discussion. Nonetheless, the results of figure 14, particularly for WS-A, are in fair agreement with the above discussion.

## 5. The power law

### 5.1. *Determination of the power law*

Historically, the determination of the power-law parameters has proved to be problematic. In the context of grid turbulence, the power law expressed by (1.2) becomes

$$\langle q^2 \rangle = A \left( \frac{U_0 t}{M} - \frac{U_0 t_0}{M} \right)^m . \tag{5.1}$$

As demonstrated by Mohamed & LaRue (1990), important uncertainties are involved in fitting a power law to measured grid data owing mainly to the sensitivity of (5.1) to parameter forcing (see also George *et al.* 2001). These problems arise because there are three parameters in (5.1) that can be varied to fit usually fewer than 10 data points that span a relatively short decay time. There is therefore a wide range of values for the power-law parameters that can match the data to virtually the same accuracy. The problem is further complicated by the need to identify the 'power-law decay range' (PLDR), which we define as the region where the turbulence decays in accordance with a power law. Mohamed & LaRue (1990) associate the power-law decay to the region where the turbulence is approximately homogeneous and isotropic. Although common wisdom would suggest that this region overlaps significantly with the PLDR, nothing in the equations suggest that they must be identical. In fact, the results of Speziale & Bernard (1992) only reach a power-law decay asymptotically for $t \to \infty$. It is therefore possible that the power law will apply for a subset of the region where the turbulence has reached an equilibrium where it is nearly homogeneous and isotropic. Both Mohamed & LaRue (1990) and Speziale & Bernard (1992) show that significant errors in the power-law parameters can arise if points outside the PLDR are used. Clearly, a method is required to determine the presence of the power law and the region within which it applies.

George *et al.* (2001) proposed an indirect means of obtaining the power law through the Taylor microscale $\lambda$. Substituting (2.2) and (5.1) into (1.7) and taking the derivative with respect to $t$, we obtain

$$\frac{\mathrm{d}\lambda^2}{\mathrm{d}t} = -\frac{10\nu}{m}\frac{U_0}{U}. \tag{5.2}$$

Therefore, if $\langle q^2 \rangle$ decays according to (5.1), then the gradient $\mathrm{d}\lambda^2/\mathrm{d}t$ must be a constant, which is inversely proportional to $m$ in the PLDR. Therefore, in addition to isolating one of the three parameters of the power law, this method also identifies if and where the turbulence decays according to (5.1). Whether $\mathrm{d}\lambda^2/\mathrm{d}t$ becomes constant is an important issue, particularly in view of the predictions of Speziale & Bernard (1992), which suggest that most wind tunnels are too short to reach the asymptotic power law yielded by their analysis.

† The number of large-eddy turnover times has been estimated here as $2t\langle\epsilon\rangle_0/\langle q^2\rangle_0$ following the suggestion by Speziale & Bernard (1992), where the initial values (subscript 0) for the dissipation and turbulence energy were taken as the values measured at $U_0 t/M = 20$ and 25 for WS-A and WS-B, respectively.

This method has been applied to results obtained by DNS, which offer small temporal increments between samples (e.g. George *et al.* 2001; Antonia & Orlandi 2004; Burattini *et al.* 2006). These authors show a region where $\mathrm{d}\lambda^2/\mathrm{d}t$ becomes constant to a close approximation in the simulations, although $m \neq -1$, which contradicts the predictions of Speziale & Bernard (1992). In the case of experimental data however, it is not practical to implement (5.2) owing to the significant noise introduced by the numerical differentiation of the data and the relatively coarse separation between measurement stations. An improved method to determine the power law from experimental data is therefore proposed here.

The method is inspired by the work of Mohamed & LaRue (1990) and of George *et al.* (2001), and hinges on two basic features. The first is that, if the turbulence decays according to (5.1) for a given range of $U_0t/M$ (the PLDR), the parameters of the power law fitted to a subset of that range should not change. The boundaries of the PLDR can therefore be probed by fitting (5.1) to different ranges of $U_0t/M$ in a manner similar to that used by Mohamed & LaRue (1990). Secondly, if the number of unknown parameters in (5.1) is reduced, the uncertainty of the fit is greatly diminished. For example, if the power law is fitted using a least-squares method with and without a prescribed value for the virtual origin, the uncertainty on $m$ is one order of magnitude smaller for the former case.

The method proposed here seeks to determine the optimum value of the virtual origin that yields a constant value for $m$ over a substantial range of $U_0t/M$. This range is then identified with the PLDR. The procedure contains the following four steps:

(*a*) Equation (5.1) is first fitted to $\langle q^2 \rangle$ over different ranges of $U_0t/M$ using several values of $U_0t_0/M$ to obtain $m_q$, where the subscript of $m$ identifies the turbulent quantity from which $m$ was estimated. The ranges for the fit extend over $U_\circ t_i/M \leqslant U_0t/M \leqslant U_0t_f/M$, where $t_i$ and $t_f$ are the minimum and maximum decay times of the range. (Since neither the intermediate nor the final stages of decay, defined by Batchelor & Townsend (1948), are reached in the present experiments, $t_f$ is kept equal to the maximum decay time available here in order to simplify the presentation of the results.)

(*b*) Determine the optimum value of $U_0t_0/M$ as the one that provides the best (defined here as the widest) plateau in the plot of $m_q$ versus $U_\circ t_i/M$.

(*c*) The minimum $U_0t/M$ location of the PLDR is equal to the smallest $U_\circ t_i/M$ before $m_q$ deviates from the plateau by more than 0.5%.

(*d*) Once $U_0t_0/M$ is obtained (step *b*) and the PLDR is identified (step *c*), the power-law can be fitted to $\langle q^2 \rangle$ to yield $m_q$ with minimal ambiguity.

The power law is fitted here with a nonlinear least-squares regression algorithm (the 'NLINFIT' routine in MatLab) to the measured data without applying a logarithmic transformation. We note that in the eventuality that the turbulence decays according to (5.1) only for $t \to \infty$, a plateau should not form over a significant range of $U_0t/M$, unless large enough decay times are reached and $m = -1$.

The data for $Sq35$ in both working sections are used to demonstrate the effectiveness of the method. Figure 16 illustrates step (*b*) with $m_q$ estimated using five different values of $U_0t_0/M$. For $Sq35$ in WS-A, $m_q$ has a nearly constant value in the range $30 \lesssim U_0t/M \lesssim 50$ with $U_0t_0/M = 7$, while a range of nearly constant $m_q$ can be observed for $34 \lesssim U_0t/M \lesssim 55$ when $U_0t_0/M = 5$ in WS-B. The deviations from a constant $m_q$ observed around $U_\circ t_i/M \gtrsim 55$ are due to the significant increase in the uncertainty of $m_q$ when the span of the region used to fit (5.1) is too short (the region $50 \lesssim U_0t/M \lesssim 80$

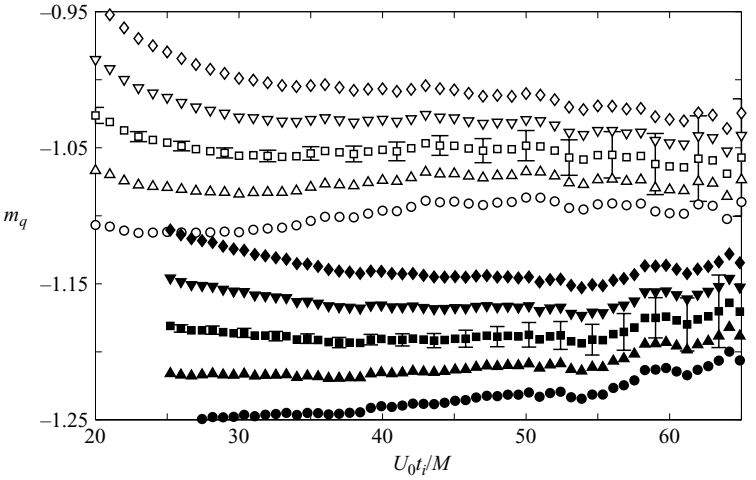


FIGURE 16. Value of $m_q$ for $Sq35$ in WS-A (open symbols) and WS-B (filled symbols) determined by fitting (5.1) to $\langle q^2 \rangle$ for $U_0 t/M \geqslant U_\circ t_i/M$ with assumed values of $U_0 t_0/M$. WS-A: $U_0 t_0/M = 5$ (○); 6 (△); 7 (□); 8 (▽); 9 (◇). WS-B: $U_0 t_0/M = 3$ (●); 4 (▲); 5 (■); 6 (▼); 7 (◆).

| WS-A | Grid | PLDR | $\frac{U_0 t_0}{M}$ | $m_q$ | $m_u$ | $m_w$ | $m_\lambda$ | $\left[\frac{U_0 t_0}{M}\right]^{LS}$ | $m_q^{LS}$ |
|---|---|---|---|---|---|---|---|---|---|
| | $Sq35$ | 30–80 | 7.0 | −1.06 | −1.06 | −1.05 | −1.05 | $7.4 \pm 0.8$ | $-1.04 \pm 0.02$ |
| | $Rd35$ | 32–80 | 6.0 | −1.18 | −1.20 | −1.17 | −1.19 | $5.7 \pm 1.3$ | $-1.19 \pm 0.04$ |
| | $Rd35b$ | 35–80 | 4.0 | −1.21 | −1.24 | −1.18 | −1.21 | $4.3 \pm 1.2$ | $-1.20 \pm 0.03$ |
| | $Rd44$ | 30–80 | 3.0 | −1.23 | −1.29 | −1.19 | −1.22 | $3.8 \pm 1.0$ | $-1.21 \pm 0.03$ |
| | $Rd44w$ | 29–80 | 6.0 | −1.17 | −1.18 | −1.17 | −1.18 | $5.9 \pm 0.7$ | $-1.18 \pm 0.02$ |
| WS-B | Grid | PLDR | $\frac{U_0 t_0}{M}$ | $m_q$ | $m_u$ | $m_w$ | $m_\lambda$ | $\left[\frac{U_0 t_0}{M}\right]^{LS}$ | $m_q^{LS}$ |
| | $Sq35$ | 34–77 | 5.0 | −1.19 | −1.18 | −1.20 | −1.18 | $4.9 \pm 1.0$ | $-1.20 \pm 0.03$ |
| | $Rd35$ | 30–77 | 5.0 | −1.23 | −1.21 | −1.24 | −1.22 | $5.2 \pm 0.7$ | $-1.22 \pm 0.02$ |
| | $Rd35b$ | 25–77 | 6.0 | −1.16 | −1.14 | −1.18 | −1.15 | $6.0 \pm 0.3$ | $-1.16 \pm 0.01$ |
| | $Rd44$ | 25–77 | 4.0 | −1.19 | −1.14 | −1.22 | −1.20 | $3.1 \pm 0.6$ | $-1.22 \pm 0.02$ |
| | $Rd44w$ | 25–77 | 7.0 | −1.10 | −1.09 | −1.10 | −1.10 | $6.8 \pm 0.5$ | $-1.10 \pm 0.02$ |

TABLE 3. Estimates of the power-law parameters from different turbulence quantities. Superscript $LS$ identifies values that yield a least-squares fit to the data without $U_0 t_0/M$ specified.

represents roughly 1.5 eddy turnover times), as observed from the growth of the error bars with increasing $U_\circ t_i/M$. The uncertainty of the values of $U_0 t_0/M$ and $m$ estimated from this method can be evaluated from the fact that the first curves above and below the one for the optimum $U_0 t_0/M$ in figure 16 could also be argued to have a significant plateau depending on the exact definition used for the 'best' plateau. This shows that the uncertainty on $U_0 t_0/M$ is $\pm 1$, which results in a $\pm 0.03$ variation in the estimate of $m$.

The power-law parameters obtained with the proposed procedure are summarized in table 3 for the different grids. The agreement between the power laws found with

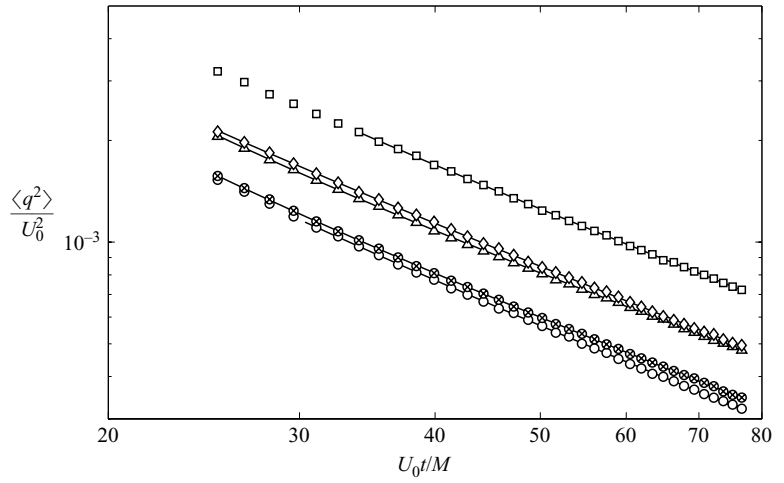


FIGURE 17. Streamwise variation of $\langle q^2 \rangle$ in WS-B. The solid lines are the power-laws fitted to the data. $Sq35$ (□), $Rd35$ (○), $Rd35b$ (⊗), $Rd44$ (◇) and $Rd44w$ (△).

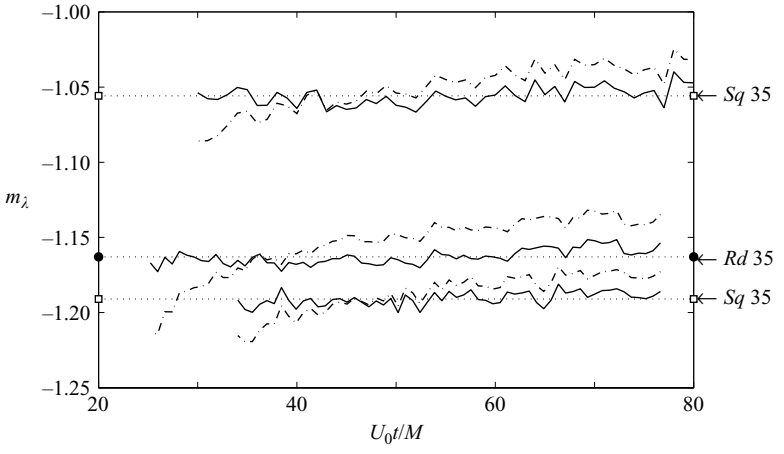


FIGURE 18. Ratio $-10\nu\,(t-t_0)\,/\lambda^2$ ($\equiv m_\lambda$) for four girds (——). The dotted horizontal lines correspond to $m_q$ for $Sq35$ (□), $Rd35b$ (○) and $Rd44$ (◇), where open and filled symbols represent data from WS-A and WS-B, respectively. Also included are the values of $m_\lambda$ obtained with an offset of 1.5 added to the optimum $U_0 t_0/M$ (— · —).

the above procedure and measured values of $\langle q^2 \rangle$ for all the grids is excellent over the PLDR (figure 17). Only the data for WS-B are shown in the figure since those for WS-A are virtually identical.

Figure 18 compares $m_q$ with the ratio $-10\nu\,(t-t_0)\,/\lambda^2\,(\equiv m_\lambda)$ for four different experimental conditions. Here, $\lambda$ was calculated with $\langle \epsilon \rangle_d$ obtained with the power-law fit found above. The local estimates of $m_\lambda$ are found to be approximately independent of $U_0 t/M$ and equal to $m_q$ for the PLDR, as required for the data to be self-consistent. Also included in figure 18 are the estimates of $m_\lambda$ obtained if the optimum value of $U_0 t_0/M$ is offset by 1.5. For these cases, $m_\lambda$ is clearly not constant. We conclude that, although using the power law to estimate $\langle \epsilon \rangle_d$ has a tendency to predispose $\lambda^2$ to grow linearly, the constancy of $m_\lambda$ is not forced and can be used

to cross-check the results. In addition, we note that the variation of $m$ with $U_0t/M$ suggested by Speziale & Bernard (1992) is not supported by the results of figures 16 and 18.

As further verification that the proposed procedure provides reliable results, the values for the power-law parameters are compared to those that produce a least-squares deviation for $\langle q^2 \rangle$ over the PLDR without $U_0t_0/M$ being specified. These results are denoted by the superscript $LS$ in table 3. Clearly, the present procedure yields a power law in good agreement with the least-squares fit. Also included in table 3 are the decay exponents obtained by fitting the power law to $\langle u^2 \rangle$ and $\langle w^2 \rangle$ with the optimum $U_0t_0/M$. The different estimates of $m$ are well within measurement uncertainty and are therefore self-consistent.

Finally, we note that the proposed procedure was also applied to the decay measurements of Comte-Bellot & Corrsin (1966), Kistler & Vrebalovich (1966), Uberoi & Wallis (1967), Gad-el-Hak & Corrsin (1974) and Mohamed & LaRue (1990). Unfortunately, the small number of measurement stations for these experiments and significant scatter prevented the power law from being determined unambiguously with our method. This, of course, demonstrates the main drawback of the procedure, which is the requirement for more measurements taken at small streamwise intervals. Nonetheless, such detailed measurements are essential if accurate and reliable estimates of the power-law parameters are required.

### 5.2. *Effects of initial conditions on the power law*

The values of $U_0t_0/M$ in table 3 are noticeably different from zero for all grid types in each working section, which does not support the suggestion of Mohamed & LaRue (1990) that $U_0t/M \simeq 0$ for all square-mesh biplane grids. In addition, the values of $m$ for the present study are, in general, different from the previously accepted values of $m = -1.25$ (Comte-Bellot & Corrsin 1966) and $-1.3$ (Mohamed & LaRue 1990). They remain, however, quite distinct from the value of $-1$ predicted by complete self-preservation (e.g. Dryden 1943).

The variation in $m$ with grid geometry is significant for WS-A, particularly between $Sq35$ and the round-rod grids. For WS-B, $m$ is nearly the same for $Sq35$, $Rd35$ and $Rd44$, while the magnitude of $m$ for $Rd44w$ is perceptibly lower ($m = -1.09$ compared to $m \simeq -1.2$; the difference cannot be accounted for by the uncertainty levels). This suggests that the anisotropy of the flow tends to increase the magnitude of $m$, since $Rd44w$ generates the most isotropic turbulence. A similar trend is observed for the results of Comte-Bellot & Corrsin (1966) with and without a secondary contraction (see their tables 1 and 3), although these authors did not consider the differences in their data to be meaningful. Furthermore, a comparison between the results for $Rd44$ and $Rd44w$ suggests that the strong periodicity present for the former leads to more negative values of $m$. This is supported by a comparison of the power-law exponents of $Rd35$ and $Rd35b$. Since $R_M$ is larger for the former, $m$ would be expected to be closer to the value of $-1$, given the expectation that $m$ tends to $-1$ for increasing $R_M$ (George 1992; Burattini *et al.* 2006). However, the presence of a more significant peak in $\phi_w(k_1)$ for $Rd35b$ compared to $Rd35$ in WS-A (figure 12*a*), highlights the stronger periodic component at the large scales for the former. Because of this difference in periodicity, the magnitude of $m$ is larger for $Rb35b$ in this case. For WS-B, similar degrees of large-scale periodicity are involved for both $Rd35$ and $Rd35b$ (figure 12*c*), and thus the value of $m$ for the latter is closer to $-1$ since $R_M$ is larger.

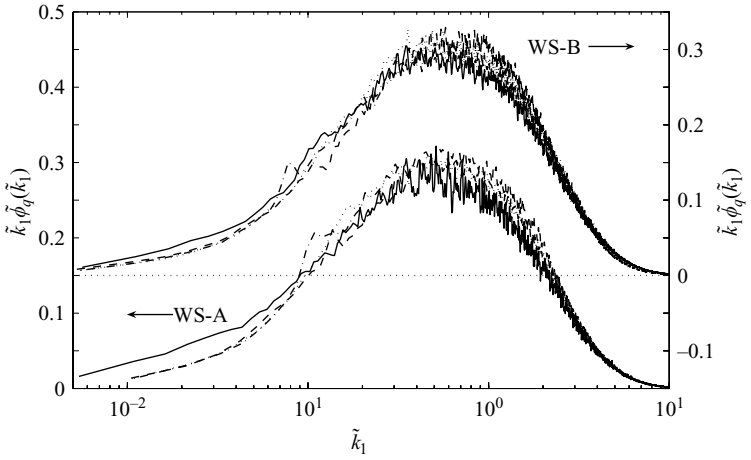


FIGURE 19. Normalized distribution of $\phi_q(k_1)$ in WS-A at $U_0t/M = 20$ and WS-B at $U_0t/M \simeq 25$ for $Sq35$ (——), $Rd35$ (— — —), $Rd44$ (— · —) and $Rd44w$ (· · ·).

There is a substantial body of evidence in the literature to suggest that the shape of $E(k)$ at low wavenumbers can determine the value of the power-law exponent at low to moderate $R_\lambda$ (e.g. Ling & Wan 1972; Chasnov 1993; Mansour & Wray 1994). This is related to the possibility that the three-dimensional spectrum (not normalized) remains invariant at the lowest wavenumbers (i.e. the spectrum retains its shape) throughout the decay for low Reynolds number, and thus, would determine the value of $m$ (e.g. Batchelor 1948). George (1992) has shown that if the three-dimensional spectrum takes the form

$$E(k, t) = C_\alpha k^\alpha \tag{5.3}$$

at small $k$ and that it is invariant throughout the decay (i.e. the constant $C_\alpha$ does not change with time), then

$$m = -(\alpha + 1)/2. \tag{5.4}$$

Although there is no evidence to suggest that $E(k)$ should be described by (5.3) for arbitrary implementations of HIT (George & Davidson 2004), this type of analysis highlights the connection between the energy distribution at low wavenumbers and the power-law decay.

It is difficult to determine the shape of $E(k)$ accurately from experimental measurements, particularly at low wavenumbers. However, the relative character of $E(k)$ for each grid can be assessed from figure 19, where the one-dimensional energy spectrum $\phi_q(k_1)$ ($\equiv \phi_u + \phi_v + \phi_w$) is plotted for each grid. The compensated semi-log plot keeps the area under the curve equal to $\langle q^2 \rangle$ so as to provide a true representation of the distribution of the energy over the relevant scales. For $Sq35$ in WS-A, $\tilde{\phi}_q(\tilde{k}_1)$ is indeed higher for $\tilde{k}_1 \leqslant 0.1$ compared to the round-rod grids. Since a lower value of $\alpha$ in (5.3) results in a high distribution of TKE at the low wavenumbers, the value of $m$ for $Sq35$, which is closer to $-1$ than the round-rod grids, is therefore consistent with (5.4) and the above discussion. The spectra for the round-rod grids are nearly identical for $\tilde{k}_1 \leqslant 0.1$, which would account for the similarity between the values of $m$ for these grids. Furthermore, the secondary contraction yields more uniformity between each grid in both the shape and magnitude of $\phi_q(k_1)$ at low wavenumbers, which shows that the contraction reduces the impact of initial conditions in grid turbulence. It is

therefore not surprising to find that the measured values of $m$ in WS-B are nearly all equal.

## 6. Conclusions

In this study, we assessed the effects of initial conditions on the characteristics of decaying turbulence using classical grids of various geometries with and without a secondary contraction. The anisotropy of the turbulence is not the same downstream of each grid and is mainly contained in the large-scale motions ($\tilde{r} > \tilde{L}_q$). However, the directional preference at the large scales does not significantly affect velocity derivative moments and vorticity fluctuations, which remain close to isotropy with no perceivable variations due to initial conditions. The secondary contraction effectively reduces the anisotropy at the large scales, while it does not adversely affect isotropy at the small scales. Although the contraction does not produce perfect isotropy, the improvement is significant and $\langle u^2\rangle/\langle w^2\rangle$ is nearly equal to one for $Rd44w$. The turbulence in WS-B is therefore considered a better approximation of HIT, and differences in the turbulence with and without the contraction highlight the effects of anisotropy at the large scales.

The collapse of the second- and third-order structure functions on equilibrium similarity variables is adequate, but not perfect. The improved isotropy in WS-B did not, in general, lead to an improvement in the collapse of the second- and third-order structure functions on equilibrium similarity variables. We conclude that, although the equations of motion are consistent with equilibrium similarity, the decay of grid turbulence only approximately supports this theory. More specifically, the present measurements corroborate the DNS results of Antonia & Orlandi (2004), who noted that the postulate of similarity at all scales is overly restrictive. Implicit in the postulate of equilibrium similarity is the assumption that the normalized structure functions are independent of $R_\lambda$ throughout the decay (for a given set of initial conditions). However, the characteristic length scales of the turbulence ($\eta$, $\lambda$ and $L$) do not remain proportional to each other as $R_\lambda$ decays, and therefore a perfect collapse is not possible unless $m = -1$, which is not found in either experiments or the DNS implementations of finite Reynolds number HIT.

Notwithstanding the low values of $R_\lambda$ ($\simeq 40$) for the present experiments, the impact of initial conditions on the second- and third-order structure functions is mainly felt at the large scales, where departures from isotropy and different levels of organization at the large scales (e.g. more or less periodicity) are most pronounced. When isotropy is improved with the use of a secondary contraction, the importance of initial conditions on the structure functions is significantly diminished. Similarly, the dependence of the power-law exponent $m$ on initial conditions, as observed in WS-A, is significantly reduced. As a whole, the current results indicate that deviations from isotropy and the presence of large-scale periodicity tend to increase the magnitude of $m$, while decay exponents closer to $-1$ are associated with turbulence where more of the energy is distributed at low wavenumbers. Based on the present results, it appears unlikely that the decay exponent for 'true' HIT would depend on initial conditions other than the dependence of $m$ on $R_\lambda$, which has been demonstrated by George (1992) and Burattini *et al.* (2006). As additional support, we note that the recent DNS data for decaying HIT by Antonia & Orlandi (2004), at comparable $R_\lambda$ to the present study, indicate that $m \simeq -1.1$. This value is close to that found for the almost perfect isotropic turbulence downstream of $Rd44w$ in WS-B. This agreement between

the decay exponent found experimentally and numerically suggests that $m = -1.1$ is the appropriate decay exponent for decaying HIT at $R_\lambda \sim 40$.

The support of the Australian Research Council is acknowledged. P.L. is grateful to Dr Burattini for many stimulating discussions and Mr Ken Sayce for the care with which he constructed the secondary contraction.

## REFERENCES

Antonia, R. A. & Orlandi, P. 2004 Similarity of decaying isotropic turbulence with a passive scalar. *J. Fluid Mech.* **505**, 123–151.

Antonia, R. A., Ould-Rouis, M., Anselmet, F. & Zhu, Y. 1997 Analogy between predictions of Kolmogorov and Yaglom. *J. Fluid Mech.* **332**, 395–409.

Antonia, R. A., Zhou, T. & Zhu, Y. 1998 Three-component vorticity measurements in a turbulent grid flow. *J. Fluid Mech.* **374**, 29–57.

Antonia, R. A., Smalley, R. J., Zhou, T., Anselmet, F. & Danaila, L. 2003 Similarity of energy structure functions in decaying homogeneous isotropic turbulence. *J. Fluid Mech.* **487**, 245–269.

Batchelor, G. K. 1947 Kolmogoroff theory of locally isotropic turbulence. *Proc. Camb. Phil. Soc.* **43**, 533–559.

Batchelor, G. K. 1948 Energy decay and self-preserving correlation functions in isotropic turbulence. *Q. Appl. Maths* **6**, 97–116.

Batchelor, G. K. 1953 *The Theory of Homogeneous Turbulence*. Cambridge University Press.

Batchelor, G. K. & Townsend, A. A. 1947 Decay of vorticity in isotropic turbulence. *Proc. R. Soc. Lond.* A **190**, 534–550.

Batchelor, G. K. & Townsend, A. A. 1948 Decay of isotropic turbulence in the initial period. *Proc. R. Soc. Lond.* A **193**, 539–558.

Benedict, L. H. & Gould, R. D. 1996 Towards better uncertainty estimates for turbulence statistics. *Exps. Fluids* **22**, 129–136.

Bennett, J. C. & Corrsin, S. 1978 Small Reynolds number nearly isotropic turbulence in a straight duct and a contraction. *Phys. Fluids* **21**, 2129–2140.

de Bruyn Kops, S. M. & Riley, J. J. 1998 Direct numerical simulation of laboratory experiments in isotropic turbulence. *Phys. Fluids* **10**, 2125–2127.

Burattini, P. & Antonia, R. A. 2005 The effect of different X-wire calibration schemes on some turbulence statistics. *Exps Fluids* **38**, 80–89.

Burattini, P., Lavoie, P., Agrawal, A., Djenidi, L. & Antonia, R. A. 2006 On the power law of decaying homogeneous isotropic turbulence at low Reynolds number. *Phys. Rev.* E **73**, 066304.

Chasnov, J. R. 1993 Similarity states of passive scalar transport in isotropic turbulence. *Phys. Fluids* **6** (2), 1036–1051.

Comte-Bellot, G. & Corrsin, S. 1966 The use of a contraction to improve the isotropy of grid-generated turbulence. *J. Fluid Mech.* **25**, 657–682.

Corrsin, S. 1963 Turbulence: experimental methods. In *Handbuch der Physik* (ed. S. Flügge & C. A. Truesdell), pp. 524–589. Springer.

Danaila, L., Anselmet, F. & Antonia, R. A. 2002 An overview of the effect of large-scale inhomogeneities on small-scale turbulence. *Phys. Fluids* **14** (7), 2475–2484.

Dryden, H. L. 1943 A review of the statistical theory of turbulence. *Q. Appl. Maths* **1**, 7–42.

Fulachier, L. & Antonia, R. A. 1983 Turbulent Reynolds and Péclet numbers re-defined. *Intl Commun. Heat Mass Transfer* **10**, 435–439.

Gad-el-Hak, M. & Corrsin, S. 1974 Measurements of the nearly isotropic turbulence behind a uniform jet grid. *J. Fluid Mech.* **62**, 115–143.

George, W. K. 1992 The decay of homogeneous isotropic turbulence. *Phys. Fluids* **4**, 1492–1509.

George, W. K. & Davidson, L. 2004 Role of initial conditions in establishing asymptotic flow behavior. *AIAA J.* **42**, 438–446.

George, W. K., Wang, H., Wollbald, C. & Johansson, T. G. 2001 Homogeneous turbulence and its relation to realizable flows. In *14th Australasian Fluid Mechanics Conference*, pp. 41–48. Adelaide University.

Huang, M.-J. & Leonard, A. 1994 Power-law decay of homogeneous turbulence at low Reynolds numbers. *Phys. Fluids* **6** (11), 3765–3775.

Kang, S. H., Chester, S. & Meneveau, C. 2003 Decaying turbulence in an active-grid-generated flow and comparisons with large-eddy simulation. *J. Fluid Mech.* **480**, 129–160.

von Kármán, T. & Howarth, L. 1938 On the statistical theory of isotropic turbulence. *Proc. R. Soc. Lond.* A **164**, 192–215.

Kistler, A. L. & Vrebalovich, T. 1966 Grid turbulence at large Reynolds numbers. *J. Fluid Mech.* **26**, 37–47.

Kolmogorov, A. N. 1941 The local structure of turbulence in incompressible viscous fluid for very large Reynolds number. *C. R. Acad. Sci. URSS* **30**, 301–305.

Korneyev, A. I. & Sedov, L. I. 1976 Theory of isotropic turbulence and its comparison with experimental data. *Fluid Mech. Sov. Res.* **5** (5), 37–48.

Lavoie, P., Burattini, P., Djenidi, L. & Antonia, R. A. 2005 Effect of initial conditions on decaying grid turbulence at low $R_\lambda$. *Exps. Fluids* **39**, 865–874.

Lavoie, P., Djenidi, L. & Antonia, R. A. 2006 Effect of initial conditions on the generation of coherent structures in grid turbulence. In *Whither Turbulence Prediction and Control Conference* (ed. H. Choi). Seoul National University.

Ling, S. C. & Wan, C. A. 1972 Decay of isotropic turbulence generated by a mechanically agitated grid. *Phys. Fluids* **15** (8), 1363–1369.

Mansour, N. N. & Wray, A. A. 1994 Decay of isotropic turbulence at low Reynolds number. *Phys. Fluids* **6** (2), 808–814.

Michelet, S., Antoine, Y., Lemoine, F. & Mahouast, M. 1998 Mesure directe du taux de dissipation de l'énergie cinétique de turbulence par vélocimétrie laser bi-composante: validation dans une turbulence de grille. *C. R. Acad. Sci. Paris II b* **326**, 621–626.

Mohamed, M. S. & LaRue, J. 1990 The decay power law in grid-generated turbulence. *J. Fluid Mech.* **219**, 195–214.

Monin, A. S. & Yaglom, A. M. 1975 *Statistical Fluid Mechanics*, vol. 2. MIT Press.

Mydlarski, L. & Warhaft, Z. 1996 On the onset of high-Reynolds-number grid-generated wind tunnel turbulence. *J. Fluid Mech.* **320**, 331–368.

Saffman, P. G. 1968 Lectures on homogeneous turbulence. In *Topics in Nonlinear Physics* (ed. N. Zabusky), pp. 485–614. Springer.

Speziale, C. G. & Bernard, P. S. 1992 The energy decay in self-preserving isotropic turbulence revisited. *J. Fluid Mech.* **241**, 645–667.

Tennekes, H. & Lumley, J. L. 1972 *A First Course in Turbulence*. The MIT Press.

Tsinober, A., Kit, E. & Dracos, T. 1992 Experimental investigation of the field of velocity gradients in turbulent flows. *J. Fluid Mech.* **242**, 169–192.

Uberoi, M. S. 1956 Effect of wind-tunnel contraction on free-stream turbulence. *J. Aero. Sci.* **23**, 754–764.

Uberoi, M. S. & Wallis, S. 1966 Small axisymmetric contraction of grid turbulence. *J. Fluid Mech.* **24**, 539–543.

Uberoi, M. S. & Wallis, S. 1967 Effect of grid geometry on turbulence decay. *Phys. Fluids* **10**, 1216–1224.

Wray, A. 1998 Decaying isotropic turbulence. *Tech. Rep.* AGARD Advisory Rep.

Zhou, T., Antonia, R. A., Lasserre, J.-J., Coantic, M. & Anselmet, F. 2003 Transverse velocity and temperature derivative measurements in grid turbulence. *Exps. Fluids* **34**, 449–459.

Zhu, Y. & Antonia, R. A. 1995 Effect of wire separation on X-probe measurements in a turbulent flow. *J. Fluid Mech.* **287**, 199–223.

Zhu, Y. & Antonia, R. A. 1996 The spatial resolution of hot-wire arrays for the measurement of small-scale turbulence. *Meas. Sci. Technol.* **7**, 1349–1359.